Simplified Steady-State Representation of Slot Synthetic Jet Actuators to Enable Numerical Optimization With Steady RANS Simulations

Sara Battaglioli, Oran James, Michael J. Gibbons, and Tim Persoons, *Member, IEEE*

***Abstract*— To address the growing energy use of data centers, waste heat recuperation offers a solution to better integrate these facilities into the broader energy system, thus facilitating a transition to the decarbonization of the energy system. The use of liquid coolants for full immersion cooling or local heat extraction from high power density components is considered for this purpose. However, heat can also be extracted by novel air cooling approaches, perhaps in combination with localized liquid cooling. To optimize heat extraction from air-cooled systems and maximize the heat grade, synthetic jets (SJs) can be used for targeted adaptive cooling in conjunction with air ducting to facilitate maximum heat recuperation potential in rack or server-mounted air-to-liquid heat exchangers. Internal server layouts can be optimized numerically, e.g., using a multiple objective genetic algorithm approach based on minimization of entropy generation rates. However, since SJs are inherently transient flow phenomena, this would require transient flow simulations, which forms a bottleneck in a numerical optimization loop. This research aims to develop a simplified steady-state representation of a synthetic jet actuator (SJA) with slot orifice using a localized body force to generate a similar time-averaged flow field to a real SJA, suitable for steady Reynolds-averaged Navier–Stokes simulations within a numerical optimization loop. Both flow fields are compared in terms of the mean flow field, jet spreading rate, and turbulence intensity distributions.**

***Index Terms*— Computational fluid dynamics (CFD), data center, energy system integration, self-similarity, server cooling, synthetic jet (SJ), unsteady flow, waste heat recuperation.**

NOMENCLATURE

A	Synthetic jet actuator area, m^2.
b	Jet half-width, m.
d_S	Width of source term volume, m.
D	Synthetic jet characteristic length, m.
f	Actuator oscillation frequency, Hz.
F_0	Synthetic jet reaction force, N.
L_0	Stroke length, m.
L_S	Streamwise length of source term volume, m.
Re	Reynolds number.
S	Momentum equation source term, Nm^{-3}.
T	Actuator oscillation period, s.
TI	Turbulence intensity.
TKE	Turbulent kinetic energy, m^2s^{-2}.
U, V	Streamwise and cross-stream velocity, m s^{-1}.
V_S	Source term volume, m^3.
x, y	Streamwise and cross-stream coordinates, m.

Greek Symbols

ϵ	Actuator diaphragm displacement, m.
ν	Fluid kinematic viscosity, m^2/s.
ρ	Fluid density, kg/m^3.

Abbreviations and Subscripts

CJ	Continuous jet.
DCJ	Dual cooling jet actuator.
SJ	Synthetic jet.
SJA	Synthetic jet actuator.

Manuscript received June 22, 2021; revised July 20, 2021; accepted August 2, 2021. Date of publication August 12, 2021; date of current version November 24, 2021. This work was supported in part by the Science Foundation Ireland under Grant 13/RC/2077_P2 and Grant SFI/15/SPP/E3125, and in part by the Irish Research Council (IRC) under Grant GOIPD/2019/666. Recommended for publication by Associate Editor K. J. Kim upon evaluation of reviewers' comments. *(Corresponding author: Tim Persoons.)*

The authors are with the Department of Mechanical, Manufacturing and Biomedical Engineering, Trinity College Dublin, University of Dublin, Dublin 2, D02 PN40 Ireland (e-mail: tim.persoons@tcd.ie).

Color versions of one or more figures in this article are available at https://doi.org/10.1109/TCPMT.2021.3104355.

Digital Object Identifier 10.1109/TCPMT.2021.3104355

I. INTRODUCTION

A. Background

IN RECENT years, the rising demand for data storage and computing resources has led to the rapid growth of more dense and powerful data centers, making them significant energy consumers worldwide. Global data center electricity demand reached around 200 TWh in 2019, accounting for about 1% of global final electricity demand [1]. In addition, the COVID-19 crisis in 2020–2021 has led to a dramatic surge in Internet traffic due to social networking, remote working, and so on so that a 60% increase in service demand is estimated by 2022 [2]. To maintain a sustainable trend, the strong growth in demand for data center services needs to be counteracted by efficiency improvements for data center infrastructures.

In a traditional data center, only 50%–60% of the total energy is used by the IT equipment itself, while thermal management and cooling systems account for about 1/3 of the total electricity consumption. New chip fabrication technologies have improved the efficiency of processors in terms of FLOPS/W, and the market share of hyperscale data centers, which operate at lower power usage effectiveness (PUE) values, has gradually increased [3]. Nevertheless, even for low

PUE hyperscale facilities, since most of the power supplied to the IT equipment is converted into heat, novel cooling technologies that enable higher grade waste heat recovery can improve the facility- and grid-level efficiency.

In the recent past, there has been an increasing thermal density of integrated circuits as package-level miniaturization proceeds. This trend necessitates innovative thermal dissipation solutions to meet these cooling requirements [4]. Bar-Cohen [5] detailed the paradigm shift from early Computer Room HVAC-like cooling techniques (1950–1975) and remote cooling with engineered thermal paths transferring heat away from the chip to the ambient air or fluid (since 1970). Bar-Cohen *et al.* [4] and Bar-Cohen [6] advised that the next generation of thermal management, "Gen3," should embed aggressive thermal management in the "chip, substrate, and/or package and directly cool the heat generation sites."

At the server level, the typical cooling system relies on forced convection from server fans that often require a significant amount of power, up to 5% of data center energy consumption. Fan convective cooling can be optimized by proper control of the fan speed depending on the actual server workload [7]–[9]. Additional strategies for server cooling could nonetheless lead to a considerable improvement in the overall efficiency of the data center.

An energy-efficient solution for data centers is hybrid cooling. Hybrid cooling implements concentrated hot spot cooling (liquid) for high heat-generating components (microprocessors and DIMM memory modules) and air cooling for low-power components (power supplies, storage disk drives, and printed circuit boards) [10]–[12]. Hybrid cooling systems have demonstrated energy savings of up to 30% [10]. However, while the use of liquid cooling is expected to increase, air cooling remains the most widespread solution [13], with further optimization potential. The waste heat produced by air cooling is underutilized due to its typical low quality. SJs are an attractive solution to increase the thermal quality of the cooling air through targeted adaptive cooling, increasing the potential for waste heat extraction. This could facilitate higher heat recuperation potential using a rack or server-mounted air-to-liquid heat exchangers [14].

B. Synthetic Jets

An SJA is a device that creates a zero net-mass-flux flow that imparts momentum to the surrounding fluid by alternating ingestion and expulsion of fluid through an orifice. Suction and ejection are due to variations of pressure in the actuator cavity generated by an oscillating diaphragm. During the ejection phase, a vortex pair or ring (depending on the shape of the orifice) sheds away from the actuator. During the ingestion phase, the vortex pair has advanced sufficiently so that it is not ingested back into the device. Hence, an SJ is formed by the harmonic formation and interaction of a train of vortices [15].

In recent years, SJ actuators have emerged as a promising solution to enhance heat transfer in electronic systems. Previous investigations into SJs impinging on heated surfaces have shown their effectiveness in disrupting the thermal boundary layer and enhancing heat transfer by increasing turbulence and mixing [16]. SJs are particularly attractive due to their simple and lightweight structure, absence of rotating parts (unlike fans), and complex piping and fluidic packaging (unlike CJs) [17].

Heat transfer enhancement from SJs has been extensively explored in the literature. Most of the studies focus on characterizing heat transfer enhancement associated with SJ impingement on heated surfaces. The cooling performance of an impinging SJ strongly depends on different parameters. For a given actuator cavity and orifice geometry, the flow field of a free, unconfined SJ is characterized by the jet Reynolds number and dimensionless stroke length [15]. The influence of these quantities has been widely investigated in the literature [18]–[22]. In general, it has been shown that for a given Reynolds and stroke length, optimal heat transfer regimes can be achieved by acting on the spacing between the actuator orifice and the heated surface. A broad review of several studies can be found in [17].

In most of the studies found in the literature, a simple geometry is considered, with an SJ in a quiescent environment impinging on a heated plate normal to the jet. Fewer studies have investigated the use of SJs for actual cooling applications. For example, de Bock *et al.* [23] and Marron and Persoons [24] explored the performance of SJs for heat sink cooling. These studies showed that SJs can provide significant cooling enhancement over natural convection and that under certain conditions, they outperform traditional fans, especially for equivalent power requirement.

The application of SJs for internal server airflow optimization has been investigated by Battaglioli *et al.* [14]. They explored the potential of using SJs associated with specifically designed baffles for enhancing the cooling efficiency in a hybrid air-/water-cooled server while improving the potential for waste heat recovery.

A computational fluid dynamics (CFD) model for the server and SJ was employed to study fluid flow and heat transfer in the server. Since SJs are inherently transient flow phenomena, transient flow simulations were required. Due to the computational cost of the process, the authors investigated only four different layouts for the SJ in the server, obtaining promising results in terms of energy savings. The airflow management in the server was improved so that the required inlet velocity from frontal fans was reduced by 50%. Also, heat recovery potential was improved, as the average outlet temperature was increased by 7 °C. Nonetheless, to perform a thorough optimization study, algorithms, such as multiple objective genetic algorithm (MOGA), need to be applied [10], [25], [26]. These kinds of optimization strategies compare the results of dozens or hundreds of simulations, gradually tuning different parameters to achieve the best solution based on the selected objectives. Hence, each simulation must have a limited computational cost to retain a reasonable computational time for the whole optimization study.

In the literature, different CFD models for SJs are found, which retains the SJ transient characteristics. Full transient period simulations of SJs are required to solve the fluid flow inside the cavity of the actuator as well as in the outer flow region. Furthermore, as the actuator membrane oscillations

generate the flow, it must also be modeled. This is done by modeling the SJA membrane as a moving boundary and introducing a deforming mesh region in its proximity [14], [27]–[29]. Because of fine grid requirements in the cavity and the small time discretization requirements due to the actuator vibration frequencies (up to kHz), the computational cost of these methods is extremely high.

In other studies, to partially reduce the computational cost and simplify the CFD model, the flow within the SJ cavity is not calculated, and the presence of the SJ actuator is simulated by a boundary condition that imposes a periodically oscillating velocity profile at the actuator orifice [30], [31]. One disadvantage of these methods is that the interaction between the actuator and the outer flow is not captured. The external fluid is virtually injected in the domain at an imposed velocity, and the zero net-mass-flux condition of the SJA is not retained. Furthermore, the transient nature of these methods makes their computational cost still too high for intense calculations, such as the MOGA optimization problem.

A possible solution to further reduce computational costs would be to move from a transient CFD model to a simplified steady-state model. Previous studies [15], [32] demonstrated that, while SJs are dominated in the near field by periodic vortex formations, in the far field, the instant velocities of a free SJ become equal to the time-averaged ones. Hence, unless a CFD study in the near field is specifically required, it is reasonable to represent an SJ as a continuous (steady) jet. The steady-state simplified model is suitable for use in a steady Reynolds-averaged Navier–Stokes (RANS) simulations within an optimization loop to make the first selection of optimal solutions. The limited number of cases selected could then be further investigated using the more advanced transient SJ models for a more physically accurate evaluation.

This article aims to present a CFD steady-state model that is able to mimic the time-averaged flow and turbulence field of a free SJ. A body force is applied at the SJ region to impart the same flow momentum as the one produced by the SJA. Parallel to the steady-state simplified model, a transient SJ CFD model is presented and is used to produce baseline results for comparison purposes.

II. Methodology

In this section, the methodology is delineated. First, the main characteristics of the SJA under consideration are described, and the characteristic parameters of free SJs are defined. Then, two CFD models for the SJA are presented. The first model (Section II-B) is a 2-D dynamic model that can reproduce the transient SJ flow field. The second model (Section II-C) is the novel steady-state model ideated by the authors to approximate the time-averaged SJ flow field in intensive computations. The first model is used to produce a baseline set of results to evaluate the second model's performance.

A. SJ Characteristics

For a given actuator geometry, a free SJ can be characterized by two dimensionless parameters [17]: the dimensionless stroke length and the jet Reynolds number. The dimensionless

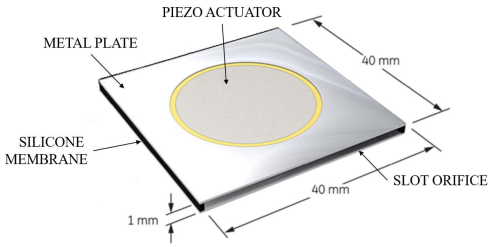

Fig. 1. Schematic of General Electric/Aavid Thermalloy DCJ [35].

stroke length is defined as $L = L_0/D$, where D is the characteristic length of the SJA orifice and L_0 is the stroke length

$$L_0 = \frac{U_0}{f} \tag{1}$$

where the characteristic velocity U_0 at the exit of the orifice is defined as follows:

$$U_0 = \frac{1}{A}\frac{1}{T}\int\int_0^{T/2} u_0 dt dA \tag{2}$$

where A is the area of the orifice, T is the oscillation period, and u_0 is the streamwise velocity at the orifice plane. Several definitions of the SJ Reynolds number can be found in the literature [17], [33], [34], depending on the chosen characteristic velocity. Since the objective of the present study is to develop a steady-state CFD model that is able to impart to the fluid the same momentum as the one produced by the SJA, the Reynolds number is defined as

$$\mathrm{Re}_m = \frac{U_m D}{\nu} \tag{3}$$

where the chosen reference velocity U_m is the jet momentum velocity, which is defined as

$$U_m = \sqrt{\frac{1}{\mathrm{TA}}\int\int_0^{T} u_0^2 dt dA}. \tag{4}$$

B. SJ Dynamic Model

The SJ actuator considered in this study is modeled on the General Electric/Aavid Thermalloy DCJ [35], shown in Fig. 1. The actuator is made of two square metal plates connected on three sides by a U-shaped silicone membrane. The fourth side is open, creating a slot orifice. The metal plates are 40 mm $\times$ 40 mm, and at rest, the slot orifice is 1 mm wide. The SJ is generated by the vibration of the two metal plates actuated via two piezo actuators. In this design, the jet flow is enhanced by the varying orifice's area during the operation cycle, i.e., the orifice expands during ingestion and contracts during expulsion [35].

The first model developed by the authors is a 2-D transient CFD representation of the DCJ. To model the vibration of the DCJ plates, the authors developed a user-defined function (UDF) that exploits the dynamic meshing model in ANSYS Fluent. The UDF allows for the walls representing the plates to move during the simulations, while the mesh around them is automatically updated. The deformation of each plate of the DCJ is modeled according to the vibration of a thin square plate with three pinned edges and one free edge in correspondence to the SJ orifice slot [36]. This assumption is

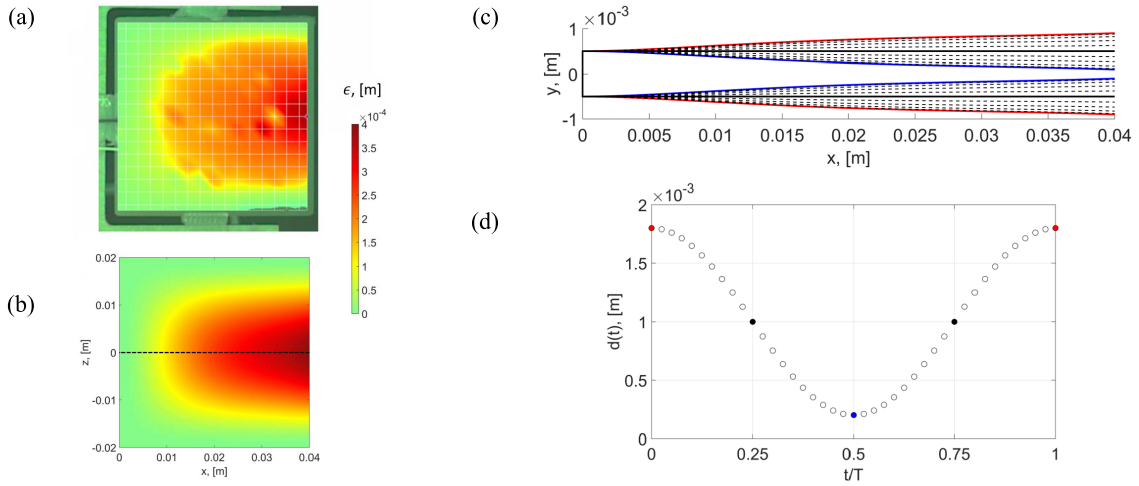

Fig. 2. Maximum DCJ metal plate deformation, comparison of (a) experimental measurement by de Bock *et al.* [35] and (b) calculated according to thin plate theory. 2-D representation of the DCJ used in the CFD model: (c) moving walls represent the vibrating plates and (d) variation of the orifice width d during one vibration cycle due to the walls' movement.

an improvement with respect to previous numerical models for the same DCJ [29], which assumed a parabolic deformation of the walls, not capturing the variation of the orifice aperture during ingestion and expulsion.

Fig. 2(a) and (b) shows a comparison of the calculated maximum displacement of the plate during a cycle with experimental measurements done using a scanning laser vibrometer by de Bock *et al.* [35].

Since the CFD model used in this study is 2-D, the DCJ is represented by its midline section [dotted line in Fig. 2(b)]; the metal plates are represented by two 40-mm moving walls, and these are connected at one side by a 1-mm-long stationary wall representing the silicone membrane and open on the opposite side to represent the orifice. Fig. 2(c) shows the 2-D representation of the DCJ during one vibration cycle. Due to the vibration of the walls, the orifice width $d(t)$ varies with time, as shown in Fig. 2(d). The time-averaged width of the orifice is $D = 1$ mm. This value is taken as characteristic length of the orifice.

Fig. 3 shows the computational domain used in the simulations. Open boundaries (pressure inlet/outlet) and a quiescent environment are assumed. The SJ actuator is parallel to the x-axis, thus producing an SJ with vortices propagating in the positive x-direction. The dimensions of the domain are 150 mm $\times$ 70 mm.

A transient, implicit model is used to solve fluid flow in the domain. A second-order upwind scheme is applied to discretize the momentum equations using the coupled algorithm for the pressure–velocity coupling. The convergence criteria for velocities and continuity are set to 10^{-6}. The k–ω SST turbulence model is used, with the near-wall mesh being sufficiently dense to have a first cell layer normalized thickness of $y^+ \leq 1$.

In the simulations, the domain is discretized using an orthogonal mesh with 1.8×10^5 cells. These values were chosen following a domain sensitivity study and a grid independence study [37]. Specifically, in the dynamic mesh region, i.e., inside and in close proximity of the DCJ, an orthogonal mesh with a sizing of 5×10^{-5} m is used. Given the oscillation

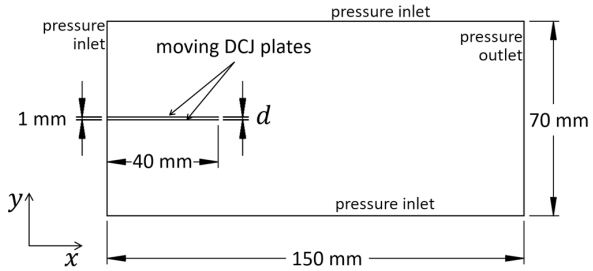

Fig. 3. Schematic of SJ dynamic model computational domain.

frequency $f = 175$ Hz, a time step $\Delta t = 5.714 \times 10^{-5}$ s, i.e., 100 steps per cycle, is assumed. These parameters allow to capture the unsteady flow and give time accurate results. Furthermore, negative cell volume during the dynamic meshing is avoided. For each simulation, 600 cycles are considered in order to reach a stable condition in the domain.

C. CJ Model

The main objective of this article is to develop a steady CFD model that would allow obtaining a flow field similar to the time-averaged one produced by the DCJ. Hence, the periodic SJ would be modeled as a CJ. The use of a steady-state model instead of the dynamic mesh model presented in Section II-B would allow for a considerable reduction of computational time.

SJ actuators are inherently zero-net-mass-flux devices, and SJs are generated imparting momentum to the surrounding fluid. Based on these considerations, the method proposed by the authors is to reproduce the time-averaged effect of the actuator by introducing a body force in the domain, able to impart the same momentum to the surrounding fluid while maintaining the zero-mass-flux condition. This is done by adding a source term S to the RANS equations governing the flow. A similar concept is used, for example, to reduce the computational cost of CFD simulations involving vortex generators [38], [39]. In these models, vortex generators are substituted by source terms that impart to the fluid the same drag and lift. Similarly, the source term S introduced here must

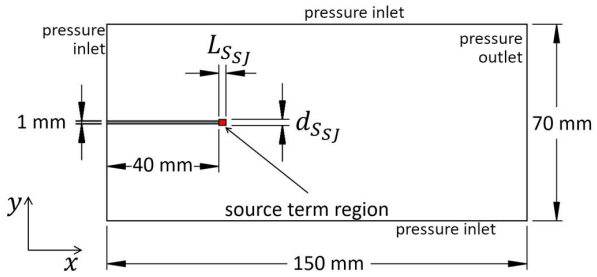

Fig. 4. Schematic of the CJ model computational domain.

impart to the fluid the same reaction force as the one produced by the SJA.

The average reaction force (F_0) in the streamwise direction of an SJA can be calculated as follows [40], [41]:

$$F_0 = \rho \frac{1}{T} \int \int_0^T u_0^2 dt dA = \rho \mathrm{AU}_m^2 \tag{5}$$

where F_0 is the total force that the source term S, active in the volume V_S, must impart to the fluid in order to mimic the effect of the SJ actuator. Therefore, the source term, expressed as force per unit volume, is defined as

$$S = \frac{F_0}{V_S} \tag{6}$$

since we are considering a 2-D model, we can rewrite the SJ source term per unit depth as

$$S = \frac{\rho \mathrm{DU}_m^2}{d_S L_S} \tag{7}$$

where D is the time average width of the orifice and d_S and L_S are the width and length of the region where the source term is active, respectively (see Fig. 4). The value of d_S and L_S must be defined through simulations in order to achieve the best agreement with the time-averaged results of the dynamic model.

Fig. 4 shows a schematic of the computational domain used in the simulations. In this case, the DCJ is treated as a solid body in the domain, which is completely closed on all four sides, unlike in the SJ model, where fluid flow inside the actuator must be solved, requiring an extremely fine mesh. The region where the source term is active is highlighted in front of the DCJ orifice. According to this layout of the domain, the streamwise direction of the SJ is along the x-axis; therefore, the source term is added to the x momentum equation in ANSYS Fluent. In this case, a computational grid with 8.9×10^4 elements is sufficient to achieve grid independence. A steady-state implicit model is used to solve fluid flow, with the same solver set up described in Section II-B.

III. Results and Discussion

In this section, the results of the SJ model (Section II-B) and the CJ model (Section II-C) are presented. In general, the steady-state model requires ~2% of the computational time of the dynamic mesh model resulting in significant time and resource-saving. This is the central motivation of this research: in order to integrate SJ numerical modeling into larger, more complex systems, such as that of a data center server, rack, or room, it is essential to minimize the computation expense of the process.

TABLE I
SJ Dynamic Model Simulation Results

	ϵ_{MAX}, [mm]	f, [Hz]	U_m, [m/s]	U_0, [m/s]	L_0/D	Re_m
SJ1	0.20	175	4.77	1.97	11.26	321
SJ2	0.30	175	6.86	2.95	16.86	462
SJ3	0.35	175	7.90	3.38	19.31	532

TABLE II
CJ Steady-State Model Input Parameters

	U_m, [m/s]	d_S, [mm]	L_S, [mm]	$\rho D U_m^2$ [N/m]
CJ1	4.77	1, 2, 3	1, 2	2.79×10^{-2}
CJ2	6.86	1, 2, 3	1, 2	5.76×10^{-2}
CJ3	7.90	1, 2, 3	1, 2	7.65×10^{-2}

Three cases are investigated for the SJ (dynamic mesh model), corresponding to three different values of the maximum deformation ϵ of the metal plates. Table I reports the stroke length L_0 [see (1)], the characteristic SJ velocity U_0 [see (2)], the momentum velocity U_m [see (4)], and Reynolds number [see (3)] for the three cases.

Velocities U_0 and U_m are calculated by numerical integration of the 2-D simulation results. For example, (2) is approximated as

$$U_0 = \frac{1}{D} \frac{1}{T} \sum_{j=1}^{N_{T/2}} \sum_{i=1}^{N_d(t_j)} u_0(y_i, t_j) \Delta y_i(t_j) \Delta t \tag{8}$$

where $N_{T/2}$ is the total number of timesteps in the half period of vibration. The total number of cells along the orifice N_d and the width of the cells Δy_i are time-dependent because of the variation of the orifice width in time due to the walls' vibration. An analogous formula is used to calculate U_m.

A parametric investigation is carried out for the CJ model (steady state) in order to evaluate its performance compared to the time-averaged SJ model results. Table II reports the input parameters used in the CJ simulations. Three values of momentum velocities, corresponding to the ones obtained for the three SJ cases (Table I), are considered. Furthermore, for each value of U_m, the width of the source region d_S is varied between 1 and 3 mm, while the length L_S is varied between 1 and 2 mm (total of six cases for each value of U_m). The value of the source term for each case is then calculated according to (8). Hence, cases CJ1, CJ2, and CJ3 correspond to cases SJ1, SJ2, and SJ3, respectively.

For each case, jet velocity and turbulence fields are analyzed, and time-averaged results from the SJ model are compared with the ones from the CJ model. Results at $x > 30D$ are considered in the comparison since the assumption of the CJ is valid strictly in the far field.

Fig. 5 shows the time-averaged centerline velocity U_C for the three SJ cases. Fig. 5(a) shows the actual velocity of the jet, while Fig. 5(b) shows the velocity normalized against the SJ momentum velocity U_m for each case. The normalized

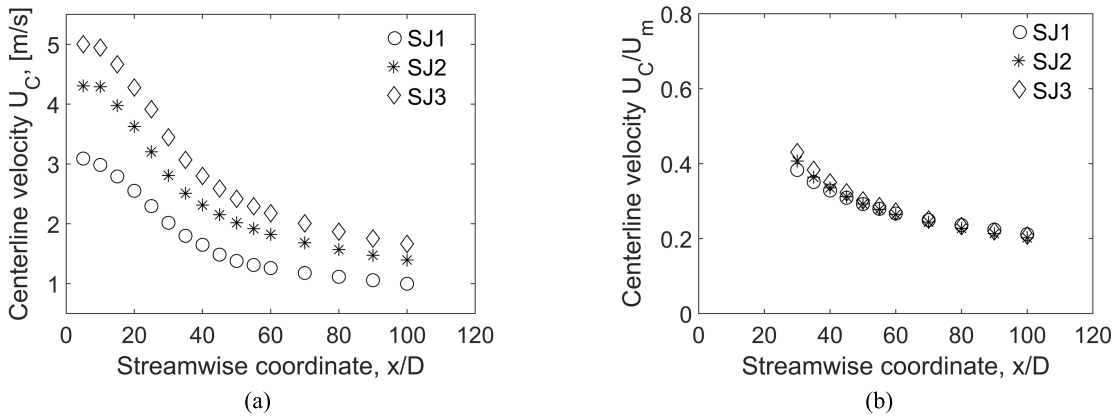

Fig. 5. SJ model time-averaged results: (a) centerline velocity and (b) normalized centerline velocity.

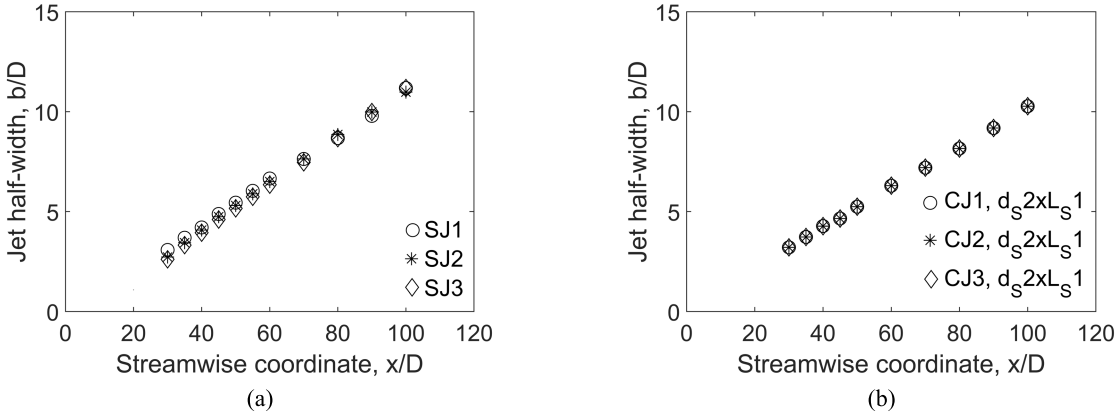

Fig. 6. Jet half-width: (a) time-averaged SJ model results and (b) CJ model results for $d_s = 2$ mm and $L_s = 1$ mm.

centerline velocity data collapse onto each other, confirming the expected jet self-similarity. The average centerline velocity decay for the SJ cases scales as $x^{-0.538}$, i.e., $r_{U_c} = -0.538$. These results are in close agreement to previous studies on planar SJs, where values between $r_{U_c} = -0.58$ [21] and $r_{U_c} = -0.5$ [33], [43] were observed.

Fig. 6 shows the jet half-width b for the SJ [Fig. 6(a)] and CJ [Fig. 6(b)] at different streamwise locations. The half-width b is conventionally calculated as the distance between the center of the jet and the location where the time-averaged streamline velocity $U = U_C/2$. As for the normalized centerline velocity, the time-averaged SJ data for half-width [Fig. 6(a)] is observed to collapse to a single line for the three cases due to the jet self-similarity. The SJ average half-width increase scales as $x^{1.05}(r_b = 1.05)$. This value agrees with values between $r_b = 0.88$ and $r_b = 1$ reported in the literature for planar SJs [15], [32], [42].

As for the SJ model, CJ model results display self-similarity both in the centerline velocity decay and in the jet half-width increase. Fig. 6(b) shows an example of the half-width profile obtained with the CJ model when $d_S = 2$ mm and $L_S = 1$ mm (note that here and in the following figures and tables, the compact notation d_sA $\times$ L_sB is used to identify a source region $d_s =$ A mm wide $\times L_s =$ B mm long). Self-similarity is observed for each value of the source term region width d_S and length L_S, with slightly different rates r_{U_C} and r_b, reported in Table III. Overall, the results are in close agreement with rates of $r_{U_C} = 1$ and $r_b = -0.5$ for planar CJs reported in the literature [43].

TABLE III
COMPARISON OF VARIATION RATES OF CENTERLINE VELOCITY, JET HALF-WIDTH, AND MAXIMUM TURBULENCE INTENSITY IN THE STREAMWISE DIRECTION FOR $x/D \geq 30$

Model		r_{U_c}	r_b	r_{TI}
SJ1				-0.59
SJ2		-0.538	1.050	-0.68
SJ3				-0.70
CJ1	$d_s1 \times L_s1$	-0.506	0.928	-0.47
	$d_s1 \times L_s2$	-0.495	0.901	-0.49
CJ2	$d_s2 \times L_s1$	-0.519	0.996	-0.44
CJ3	$d_s2 \times L_s2$	-0.507	0.961	-0.46
	$d_s3 \times L_s1$	-0.519	0.949	-0.46
	$d_s3 \times L_s2$	-0.510	0.958	-0.42

Fig. 7(a) shows a comparison of the averaged normalized centerline velocity profile between the SJ model and the CJ model. For each case, the average between cases SJ1, SJ2, and SJ3 and CJ1, CJ2, and CJ3 is displayed. The best agreement in terms of velocity field between the SJ model and CJ model results is found when $d_S = 2$ mm and $L_S = 1$ mm. Fig. 7(b) shows the comparison between the SJ and CJ results for the streamwise velocity at different locations x/D, from 40 to 100 in steps of 20. SJ2 and CJ2 are reported as an example. At $x/D = 30$, the CJ model slightly underestimates the peak velocity by a 7% error; however, for higher values of x/D,

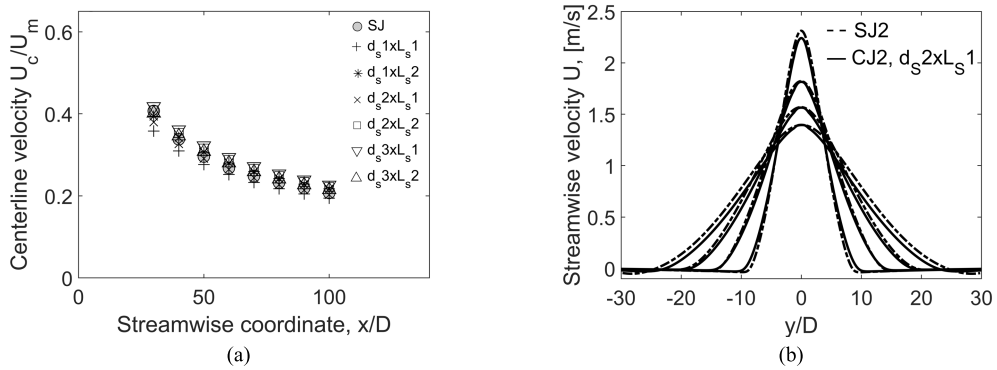

Fig. 7. SJ versus CJ results: (a) normalized centerline velocity and (b) streamwise velocity at downstream locations $x/D = 40$, 60, 80, and 100.

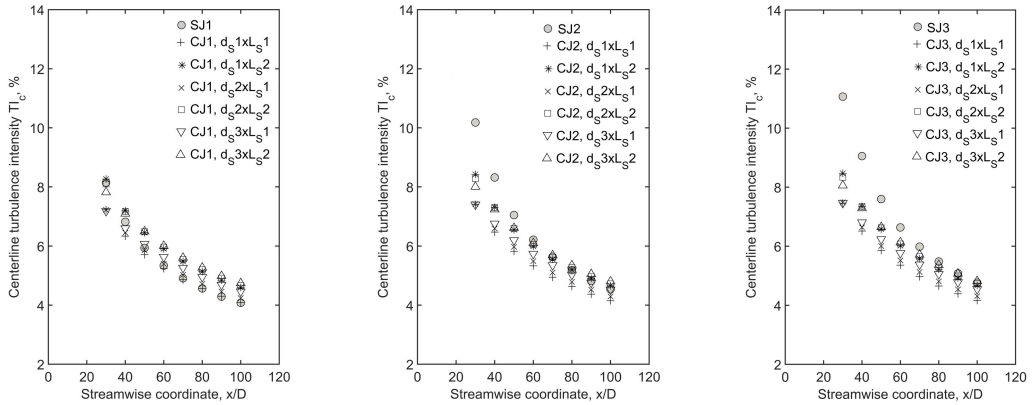

Fig. 8. Centerline turbulence intensity: (a) time-averaged SJ1 versus CJ1, (b) time-averaged SJ2 versus CJ2, and (c) time-averaged SJ3 versus CJ3.

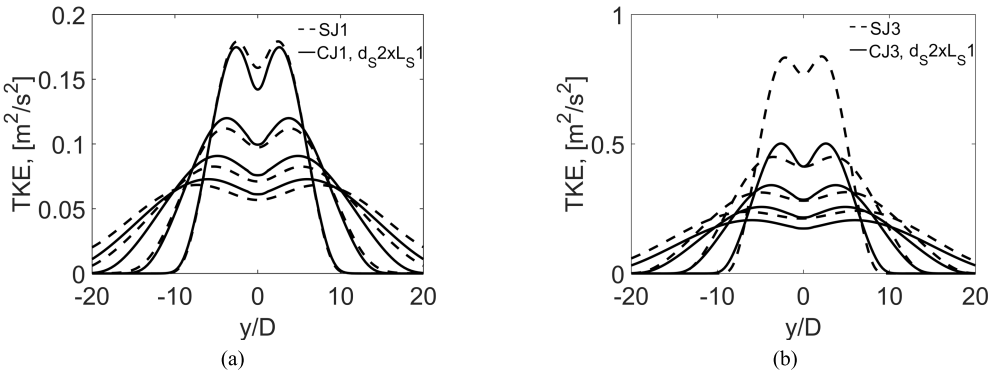

Fig. 9. Turbulent kinetic energy profiles at locations $x/D = 40$, 60, 80, and 100: (a) time-averaged SJ1 versus CJ1 results and (b) time-averaged SJ3 versus CJ3 results.

the SJ and CJ results show a good agreement along the whole jet width, with a peak velocity error <3% for $x/D \geq 40$, and <1% for $x/D \geq 50$. Similar results are registered for SJ1 versus CJ1 and SJ3 versus CJ3, with maximum errors at $x/D = 30$ of 8% and 12%, respectively.

Fig. 8 shows the turbulence intensity at the center of the jet predicted by the SJ model compared to the one predicted by the CJ model. The turbulence intensity for each case is calculated as $\text{TI} = u'/U_m$, where the turbulent velocity fluctuations are given by $u' = (2/3\ \text{TKE})^{1/2}$. Fig. 8(a)–(c) shows the results for cases SJ1 versus CJ1, SJ2 versus CJ2, and SJ3 versus CJ3, respectively. Unlike for centerline velocity and jet half-width, SJ turbulence intensity results do not collapse onto a single curve. In fact, higher values of turbulence intensity are observed for higher U_m, i.e., at higher Reynolds Re_m. Also, the rate of decay varies between the three cases, from $x^{-0.59}$ to $x^{-0.7}$, as reported in Table III. On the contrary, for each combination of $d_S \times L_S$, CJ turbulence intensity results show self-similarity across the three values of U_m. While TI values are different for each $d_S \times L_S$, the rate of decay is almost unchanged for all the simulations, varying between $x^{-0.42}$ and $x^{-0.49}$. Because of the different behavior of the SJ and CJ models in predicting the turbulence intensity, TI in case SJ1 is closely matched by the one predicted by CJ1 models for $x/D \geq 30$; however, CJ2 and CJ3 underestimate the TI of cases SJ2 for $x/D < 50$ and SJ3 for $x/D < 80$, respectively.

Turbulent kinetic energy profiles at different locations x/D from 40 to 100 in steps of 20 are shown in Fig. 9. In agreement with what observed for the turbulence intensity, the CJ model is able to reproduce the SJ results quite accurately in the

first case [SJ1 versus CJ1, Fig. 9(a)], with a 10.5% error at the centerline for $x/D < 40$, decreasing to a 2.5% error for $x/D \geq 50$. On the contrary, for SJ2 and SJ3, the turbulence levels are underestimated at low x/D [see Fig. 9(b)], with over 50% error at the centerline for $x/D < 40$, decaying to a 15% error for $x/D > 60$.

IV. Conclusion

The aim of this article was to develop a simplified steady-state CFD model that is able to mimic the time-averaged flow field produced by an SJA in the far field, i.e., for $x/D \geq 30$. The model is meant to be used in intensive calculations, such as the ones required when performing optimization studies involving a high number of design points, provided that a detailed analysis in the close field is not of interest.

In the simplified model proposed by the authors, described in Section II-C, the transient SJ is replaced by a steady, CJ is produced by a localized body force that imparts to the fluid the same momentum as the one produced by the SJA over a vibration period. To validate the CJ model, results were compared with the ones produced using a transient SJ model, described in Section II-B.

Results were compared for three different values of the momentum velocity U_m ($\propto \mathrm{Re}_m$) of the SJ, corresponding to three different values of the body force applied in the CJ model. In addition, for the CJ model, a parametric investigation for each value of the velocity was performed to determine the dimensions of the source term region.

The CJ approach has been shown to provide an initial quasi-approximation of its dynamic mesh model (SJ) counterpart for far-field shape, centerline velocity, and half-width over the investigated range of Re_m. The best agreement in the velocity field was found when the source term region was $d_s = 2$ mm wide $\times L_s = 1$ mm long, with 12% maximum error in the centerline velocity at positions closer to the SJA orifice ($x/D \sim 30$), decaying to $<1\%$ errors for $x/D > 50$.

Comparison of the turbulence field showed a good agreement at lower Re_m, i.e., for case SJ1 and its counterpart CJ1. However, the agreement has been shown to deteriorate at higher Re_m. In particular, the turbulence intensity and kinetic energy from SJ2 and SJ3 were significantly underestimated by the CJ model for $x/D < 50$ and $x/D < 80$, respectively. A possible solution for this shortcoming would be to introduce, in further development of the CJ model, a turbulence source term acting alongside the body force source term, which would be proportional to the SJ Reynolds number. Other future work includes the improvement of the source term model by further optimizing the choice of the volume V_S, perhaps linking its value to the stroke length L_0. Also, in the proposed model, S was constant in the volume V_S, while an optimized distribution might offer a better representation of the SJ.

Acknowledgment

The authors would like to thank the support of the DJEI/DES/SFI/HEA Irish Centre for High-End Computing (ICHEC) for the provision of computational facilities and support.

References

[1] E. Masanet, A. Shehabi, N. Lei, S. Smith, and J. Koomey, "Recalibrating global data center energy-use estimates," *Science*, vol. 367, no. 6481, pp. 984–986, Feb. 2020, doi: 10.1126/science.aba3758.

[2] IEA. (2020). *Data Centres and Data Transmission Networks*, IEA, Paris, France. [Online]. Available: https://www.iea.org/reports/data-centres-and-data-transmission-networks

[3] N. Jones, "How to stop data centres from gobbling up the world's electricity," *Nature*, vol. 561, no. 7722, pp. 163–166, 2018, doi: 10.1038/d41586-018-06610-y.

[4] A. Bar-Cohen *et al.*, "Challenges and opportunities in Gen3 embedded cooling with high-quality microgap flow," in *Proc. Int. Conf. Electron. Packag. iMAPS All Asia Conf. (ICEP-IAAC)*, Apr. 2018, pp. K-1–K-12, doi: 10.23919/ICEP.2018.8374353.

[5] A. Bar-Cohen, "Gen 3 'embedded' cooling: Key enabler for energy efficient data centers," *IEEE Trans. Compon., Packag., Manuf. Technol.*, vol. 7, no. 8, pp. 1206–1211, Aug. 2017, doi: 10.1109/TCPMT.2017.2724922.

[6] A. Bar-Cohen, "Towards embedded cooling-Gen 3 thermal packaging technology," in *Encyclopedia of Thermal Packaging*. 2014, pp. 367–398, doi: 10.1142/9789814678063_0016.

[7] Z. Wang *et al.*, "Optimal fan speed control for thermal management of servers," in *Proc. ASME InterPACK*, vol. 2, 2009, pp. 709–719, doi: 10.1115/InterPACK2009-89074.

[8] X. Han and Y. Joshi, "Energy reduction in server cooling via real time thermal control," in *Proc. 28th Annu. IEEE Semiconductor Thermal Meas. Manage. Symp. (SEMI-THERM)*, Mar. 2012, pp. 20–27, doi: 10.1109/STHERM.2012.6188829.

[9] Q. Zheng, Z. Ping, S. Soares, Y. Hu, and Z. Gao, "An optimized active disturbance rejection approach to fan control in server," *Control Eng. Pract.*, vol. 79, pp. 154–169, Oct. 2018, doi: 10.1016/j.conengprac.2018.07.003.

[10] A. Sakanova, S. Alimohammadi, J. McEvoy, S. Battaglioli, and T. Persoons, "Multi-objective layout optimization of a generic hybrid-cooled data centre blade server," *Appl. Thermal Eng.*, vol. 156, pp. 514–523, Jun. 2019, doi: 10.1016/j.applthermaleng.2019.04.071.

[11] M. Iyengar *et al.*, "Server liquid cooling with chiller-less data center design to enable significant energy savings," in *Proc. 28th Annu. IEEE Semiconductor Thermal Meas. Manage. Symp. (SEMI-THERM)*, Mar. 2012, pp. 212–223, doi: 10.1109/STHERM.2012.6188851.

[12] L. Gibbons, B. Coyne, D. Kennedy, and S. Alimohammadi, "A techno-economic analysis of current cooling techniques in Irish data centres," in *Proc. 25th Int. Workshop Thermal Investigations ICs Syst. (THERMINIC)*, Sep. 2019, pp. 1–6, doi: 10.1109/THERMINIC.2019.8923482.

[13] S. V. Garimella, T. Persoons, J. A. Weibel, and V. Gektin, "Electronics thermal management in information and communications technologies: Challenges and future directions," *IEEE Trans. Compon., Packag., Manuf. Technol.*, vol. 7, no. 8, pp. 1191–1205, Aug. 2017, doi: 10.1109/TCPMT.2016.2603600.

[14] S. Battaglioli, A. Sakanova, and T. Persoons, "Hybrid-cooled server optimization for air-side waste heat recovery using passive and active flow control," in *Proc. 25th Int. Workshop Thermal Investigations ICs Syst. (THERMINIC)*, Sep. 2019, pp. 1–6, doi: 10.1109/THERMINIC.2019.8923803.

[15] B. L. Smith and A. Glezer, "The formation and evolution of synthetic jets," *Phys. Fluids*, vol. 10, no. 9, pp. 2281–2297, Sep. 1998, doi: 10.1063/1.869828.

[16] G. Krishan *et al.*, "Synthetic jet impingement heat transfer enhancement–A review," *Appl. Thermal Eng.*, vol. 149, pp. 1305–1323, Feb. 2019, doi: 10.1016/j.applthermaleng.2018.12.134.

[17] A. Glezer and M. Amitay, "Synthetic jets," *Annu. Rev. Fluid Mech.*, vol. 34, no. 1, pp. 503–529, 2002, doi: 10.1146/annurev.fluid.34.090501.094913.

[18] A. McGuinn, R. Farrelly, T. Persoons, and D. B. Murray, "Flow regime characterisation of an impinging axisymmetric synthetic jet," *Exp. Thermal Fluid Sci.*, vol. 47, pp. 241–251, May 2013, doi: 10.1016/j.expthermflusci.2013.02.003.

[19] P. Valiorgue, T. Persoons, A. McGuinn, and D. B. Murray, "Heat transfer mechanisms in an impinging synthetic jet for a small jet-to-surface spacing," *Exp. Thermal Fluid Sci.*, vol. 33, no. 4, pp. 597–603, Apr. 2009, doi: 10.1016/j.expthermflusci.2008.12.006.

[20] C. S. Greco, G. Paolillo, A.Ianiro, G. Cardone, and L. de Luca, "Effects of the stroke length and nozzle-to-plate distance on synthetic jet impingement heat transfer," *J. Fluid Mech.*, vol. 810, pp. 25–59, Feb. 2018, doi: 10.1016/j.ijheatmasstransfer.2017.09.118.

[21] M. Hatami, F. Bazdidi-Tehrani, A. Abouata, and A. Mohammadi-Ahmar, "Investigation of geometry and dimensionless parameters effects on the flow field and heat transfer of impingement synthetic jets," *Int. J. Thermal Sci.*, vol. 127, pp. 41–52, May 2018, doi: 10.1016/j.ijthermalsci.2018.01.011.
[22] X. He, J. A. Lustbader, M. Arik, and R. Sharma, "Heat transfer characteristics of impinging steady and synthetic jets over vertical flat surface," *Int. J. Heat Mass Transf.*, vol. 80, pp. 825–834, Jan. 2015, doi: 10.1016/j.ijheatmasstransfer.2014.08.006.
[23] H. P. de Bock, P. Chamarthy, J. L. Jackson, and B. Whalen, "Investigation and application of an advanced dual piezoelectric cooling jet to a typical electronics cooling configuration," in *Proc. 13th InterSociety Conf. Thermal Thermomech. Phenomena Electron. Syst.*, May 2012, pp. 1387–1394, doi: 10.1109/ITHERM.2012.6231582.
[24] C. Marron and T. Persoons, "Experimental optimisation of the thermal performance of impinging synthetic jet heat sinks," in *Proc. J. Phys., Conf.*, Jul. 2014, vol. 525, Art. no. 012027, doi: 10.1088/1742-6596/525/1/012027.
[25] A. Sakanova, S. Alimohammadi, J. McEvoy, and T. Persoons, "Hybrid-cooled data center server layout optimization for air-side heat recovery," in *Proc. 24rd Int. Workshop Thermal Investigations ICs Syst. (THERMINIC)*, Sep. 2018, pp. 1–4, doi: 10.1109/THERMINIC.2018.8593309.
[26] S. Battaglioli, A. Sakanova, and T. Persoons, "Numerical convective heat transfer analysis of a hybrid-cooled data center blade server," in *Proc. 18th IEEE Intersociety Conf. Thermal Thermomech. Phenomena Electron. Syst. (ITherm)*, May 2019, pp. 276–282, doi: 10.1109/ITHERM.2019.8757279.
[27] A. Miró, M. Soria, J. C. Cajas, and I. Rodríguez, "Numerical study of heat transfer from a synthetic impinging jet with a detailed model of the actuator membrane," *Int. J. Thermal Sci.*, vol. 136, pp. 287–298, Feb. 2019, doi: 10.1016/j.ijthermalsci.2018.10.017.
[28] D. P. Rizzetta, M. R. Visbal, and M. J. Stanek, "Numerical investigation of synthetic-jet flowfields," *AIAA J.*, vol. 37, no. 8, pp. 919–927, Aug. 1999, doi: 10.2514/2.811.
[29] D. Jang and K.-S. Lee, "Flow characteristics of dual piezoelectric cooling jets for cooling applications in ultra-slim electronics," *Int. J. Heat Mass Transf.*, vol. 79, pp. 201–211, Dec. 2014, doi: 10.1016/j.ijheatmasstransfer.2014.08.013.
[30] D. Velasco, O. López Mejia, and S. Laín, "Numerical simulations of active flow control with synthetic jets in a darrieus turbine," *Renew. Energy*, vol. 113, pp. 129–140, Dec. 2017, doi: 10.1016/j.renene.2017.05.075.
[31] Y. Zhang, P. Li, and Y. Xie, "Numerical investigation of heat transfer characteristics of impinging synthetic jets with different waveforms," *Int. J. Heat Mass Transf.*, vol. 125, pp. 1017–1027, Oct. 2018, doi: 10.1016/j.ijheatmasstransfer.2018.04.120.
[32] B. L. Smith and G. W. Swift, "A comparison between synthetic jets and continuous jets," *Experim. Fluids*, vol. 34, no. 4, pp. 467–472, Apr. 2003, doi: 10.1007/s00348-002-0577-6.
[33] R. Holman, Y. Utturkar, R. Mittal, B. L. Smith, and L. Cattafesta, "Formation criterion for synthetic jets," *AIAA J.*, vol. 43, no. 10, pp. 2110–2116, Oct. 2005, doi: 10.2514/1.12033.
[34] A. Arshad *et al.*, "Synthetic jet actuators for heat transfer enhancement–A critical review," *Int. J. Heat Mass Transf.*, vol. 146, Jan. 2020, Art. no. 118815, doi: 10.1016/j.ijheatmasstransfer.2019.118815.
[35] H. P. de Bock, T. Persoons, and K. Bodla, "Particle image velocimetry study on dual cooling jet flows," in *Proc. 15th IEEE Intersociety Conf. Thermal Thermo Mech. Phenomena Electron. Syst. (ITherm)*, May 2016, pp. 1366–1372, doi: 10.1109/ITHERM.2016.7517708.
[36] S. Timoshenko, *Theory of Plates and Shells*. New York, NY, USA: McGraw-Hill, 1959.
[37] E. Collins, "Optimisation of a hybrid cooled data centre server for energy recuperation," M.S. thesis, School Eng., Trinity College Dublin, Dublin, Ireland, 2020.
[38] J. C. Dudek, "Modeling vortex generators in a Navier-Stokes code," *AIAA J.*, vol. 49, no. 4, pp. 748–759, Apr. 2011, doi: 10.2514/1.J050683.
[39] M. Manolesos, G. Papadakis, and S. G. Voutsinas, "Revisiting the assumptions and implementation details of the BAY model for vortex generator flows," *Renew. Energy*, vol. 146, pp. 1249–1261, Feb. 2020, doi: 10.1016/J.RENENE.2019.07.063.
[40] P. Gil, "Synthetic jet Reynolds number based on reaction force measurement," *J. Fluids Struct.*, vol. 81, pp. 466–478, Aug. 2018, doi: 10.1016/J.JFLUIDSTRUCTS.2018.05.011.
[41] P. Gil and E. Smyk, "Synthetic jet actuator efficiency based on the reaction force measurement," *Sens. Actuators A, Phys.*, vol. 295, pp. 405–413, Aug. 2019, doi: 10.1016/j.sna.2019.06.011.
[42] A. Agrawal and G. Verma, "Similarity analysis of planar and axisymmetric turbulent synthetic jets," *Int. J. Heat Mass Transf.*, vol. 51, nos. 25–26, pp. 6194–6198, Dec. 2008, doi: 10.1016/j.ijheatmasstransfer.2008.04.011.
[43] S. Pope, *Turbulent Flows*. Cambridge, U.K.: Cambridge Univ. Press, 2000, doi: 10.1017/CBO9780511840531.

Sara Battaglioli received the Ph.D. degree in engineering from Trinity College Dublin, Dublin, Ireland, in 2018.

She is currently a CONNECT Research Fellow with the Department of Mechanical, Manufacturing and Biomedical Engineering, Trinity College Dublin. Her main expertise is in advanced computational fluid dynamics (CFD) and heat transfer. Her research activities include multiscale convective heat transfer for electronics thermal management using enhanced air and liquid cooling, active flow control for sustainable energy technologies, and improved waste heat recovery.

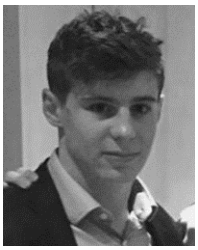

Oran James received the master's (M.A.I.) degree in mechanical and manufacturing engineering from the Department of Mechanical, Manufacturing and Biomedical Engineering, Trinity College Dublin, Dublin, Ireland, in 2021. His final year research project (2020–2021) focused on developing a steady-state representation using Reynolds-averaged Navier–Stokes (RANS) computational fluid dynamics (CFD) modeling of a synthetic jet actuator for use in server cooling optimization.

Michael J. Gibbons received the Ph.D. degree in engineering from Trinity College Dublin, Dublin, Ireland, in 2017.

He is currently an Irish Research Council Fellow with the Department of Mechanical, Manufacturing and Biomedical Engineering, Trinity College Dublin. He has authored over 20 refereed journal and conference publications. His research focuses on microscale multiphase heat transfer and energy recovery from data centers through the development of innovative waste heat transportation and conversion technologies to fight climate change.

Tim Persoons (Member, IEEE) received the M.Sc. degree in mechanical engineering and the Ph.D. degree in engineering from KU Leuven, Leuven, Belgium, in 1999 and 2006, respectively.

He is currently an Associate Professor with the Department of Mechanical and Manufacturing Engineering, Trinity College Dublin, Dublin, Ireland, and a Visiting Faculty Member at the NSF I/UCRC Cooling Technologies Research Center, Purdue University West Lafayette, IN, USA. His research focuses on thermal management of electronics systems, from cooling microscale devices to waste heat recuperation and sustainable energy system integration of data centers.